Solution Structure of the (+)-cis-anti-Benzo[a]pyrene-dA ([BP]dA) Adduct Opposite dT in a DNA Duplex†

9 AUTHORS, INCLUDING:

Bing Mao
Merck
54 PUBLICATIONS **1,106** CITATIONS

SEE PROFILE

Andrey A Gorin
Oak Ridge National Laboratory
69 PUBLICATIONS **3,102** CITATIONS

SEE PROFILE

Brian Hingerty
Tennessee Wesleyan College
144 PUBLICATIONS **4,859** CITATIONS

SEE PROFILE

Nicholas E Geacintov
New York University
432 PUBLICATIONS **12,020** CITATIONS

SEE PROFILE

Solution Structure of the (+)-*cis-anti*-Benzo[*a*]pyrene-dA ([BP]dA) Adduct Opposite dT in a DNA Duplex†

Bing Mao,‡ Zhentian Gu,‡ Andrey Gorin,‡ Junxin Chen,§ Brian E. Hingerty,‖ Shantu Amin,⊥ Suse Broyde,○ Nicholas E. Geacintov,‡ and Dinshaw J. Patel*,‡

Cellular Biochemistry and Biophysics Program, Memorial Sloan-Kettering Cancer Center, New York, New York 10021, Chemistry and Biology Departments, New York University, New York, New York 10003, Life Sciences Research Division, Oak Ridge National Laboratory, Oak Ridge, Tennessee 37831, and American Health Foundation, Valhalla, New York 10595

ABSTRACT: Minor adducts, derived from the covalent binding of *anti*-benzo[*a*]pyrene-7,8-dihydroxy-9,-10-epoxide to cellular DNA, may play an important role in generating mutations and initiating cancer. We have applied a combined NMR−computational approach including intensity based refinement to determine the solution structure of the minor (+)-*cis-anti*-[BP]dA adduct positioned opposite dT in the d(C1−T2−C3−T4−C5−[BP]A6−C7−T8−T9−C10−C11)·(d(G12−G13−A14−A15−G16−T17−G18−A19−G20−A21−G22) 11-mer duplex. The BP ring system is intercalated toward the 5′-side of the [BP]-dA6 lesion site without disrupting the flanking Watson−Crick dC5·dG18 and [BP]dA6·dT17 base pairs. This structure of the (+)-*cis-anti*-[BP]dA·dT 11-mer duplex, containing a bay region benzo[*a*]pyrenyl [BP]dA adduct, is compared with the corresponding structure of the (+)-*trans-anti*-[BPh]dA·dT 11-mer duplex (Cosman et al., *Biochemistry 32*, 12488−12497, 1993), which contains a fjord region benzo[*c*]-phenanthrenyl [BPh]dA adduct with the same *R* stereochemistry at the linkage site. The carcinogen intercalates toward the 5′-direction of the modified strand in both duplexes (the adduct is embedded within the same sequence context) with the buckling of the Watson−Crick [BP]dA6·dT17 base pair more pronounced in the (+)-*cis-anti*-[BP]dA·dT 11-mer duplex compared to its Watson−Crick [BPh]dA·dT17 base pair in the (+)-*trans-anti*-[BPh]dA·dT 11-mer duplex. The available structural studies of covalent polycyclic aromatic hydrocarbon (PAH) carcinogen-DNA adducts point toward the emergence of a general theme where distinct alignments are adopted by PAH adducts covalently linked to the N^6 of adenine when compared to the N^2 of guanine in DNA duplexes. The [BPh]dA and [BP]dA N^6-adenine adducts intercalate their polycyclic aromatic rings into the helix without disruption of their modified base pairs. This may reflect the potential flexibility associated with the positioning of the covalent tether and the benzylic ring of the carcinogen in the sterically spacious major groove. By contrast, such an intercalation without modified base pair disruption option appears not to be available to [BP]dG N^2-guanine adducts where the covalent tether and the benzylic ring are positioned in the more sterically crowded minor groove. In the case of [BP]dG adducts, the benzopyrenyl ring is either positioned in the minor groove without base pair disruption, or if intercalated into the helix, requires disruption of the modified base pair and displacement of the bases out of the helix.

Benzo[*a*]pyrene is an ubiquitous environmental precarcinogen produced by incomplete combustion of fossil fuels and is found in automobile exhaust, tobacco smoke, and even as a contaminant in foods (*1−3*). Metabolic activation (reviewed in *1*) leads to the formation of a number of reactive and genotoxic bay region 7,8-dihydroxy-9,10-epoxide-7,8,9,-10-tetrahydrobenzo[*a*]pyrene diol epoxide derivatives. The (+)-7*R*,8*S*,9*S*,10*R* stereoisomer, (+)-anti BPDE, is highly tumorigenic in rodents, while the mirror image (−)-7*S*,8*R*,9*R*,-10*S* enantiomer, (−)-*anti*-BPDE, is inactive (*4−5*). Both (+)-and (−)-*anti*-BPDEs react with native DNA to form various covalent reaction products (*6−7*) via *trans* and *cis* addition to the exocyclic amino groups of guanine (N^2-dG) and adenine (N^6-dA) to the C^{10} position of *anti*-BPDE. While the reaction yields of [BP]dG guanine adducts are greater than those of [BP]dA adenine adducts, evidence is accumulating that adenine adducts may play a significant role in carcinogenesis associated with polynuclear aromatic diol epoxides (*8−10*).

It is well-established that both *anti*-BPDE enantiomers can cause mutations in prokaryotic (*11−14*) and eukaryotic (*15−18*) genes. Mutations induced by covalent BPDE−DNA adducts in mammalian genes may play an important role in chemical carcinogenesis (*19−20*). The relative contributions of the major [BP]dG and the minor [BP]dA lesions to the mutagenic potentials of (+)- and (−)-*anti*-BPDE are still not well-understood.

A particularly interesting finding is that the proportions of mutations at adenine residues in the *hprt* gene in Chinese hamster V79 cells increases as the *anti*-BPDE dosages are decreased to physiologically more relevant lower levels (*15−16, 18*). At all dosages, base substitutions were prevalent, and smaller levels of exon deletions and frameshift mutations were reported. The fascinating observations were made that almost all of the mutations involving guanine occurred on the nontranscribed strand, while the mutations observed at adenine occurred with twice the frequency on the transcribed relative to the nontranscribed strand. These results suggest that the observed strand specificities for (+)-*anti*-BPDE induced mutagenesis may result from the preferential excision of *anti*-[BP]dG lesions from the transcribed strand; on the other hand, *anti*-[BP]dA adducts do not seem to be excised as efficiently from the transcribed strand as the *anti*-[BP]dG lesions (*16*). Recently, it has been shown that the efficiency of excision repair of [BP]dG lesions in cellular double-stranded DNA may depend in a critical manner on the structural characteristics of the stereoisomeric duplexes (*21*). It is, therefore, of great interest to also characterize the structures of the stereoisomeric [BP]dA and related adenine adducts.

Recently, considerable progress has been made in determining the NMR solution structures of a number of [BP]-dG, [BP]dA, and related adducts by high-resolution NMR techniques. Diverse stereochemical- and base-sequence-dependent patterns of adduct conformations are emerging that have led to new insights into the relationship between structure and function (reviewed in *22*). Initial studies of an adduct derived from the binding of the (+)-1*R*,2*S*,3*S*,4*R* enantiomer of 1,2-hydroxyl-3,4-dihydroxyl-1,2,3,4-tetrahydrobenzo[*c*]phenanthrene (BPhDE) to N6-dA (1*R* (+)-*trans*-adduct) showed that the aromatic residue (BPh) is intercalated on the 5′-side of the modified adenine residue with all base pairs in the 11-mer duplex in a Watson−Crick alignment (*23*). A similar conformation is observed in the case of steroisomeric 1*S*-(−)-*trans*-[BPh]dA adduct, except that the BPh residue is intercalative on the 3′-side of the modified adenine residue (*24*). The high-resolution NMR solution structure of the (+)-*trans-anti*-[BP]-dA adduct with 10*S* stereochemistry at the linkage site has been obtained in a DNA duplex in which the adducted dA is mismatched with dG; both a major conformer (*25*) and a minor conformer (*26*) have been delineated in this mismatched duplex; in both cases the aromatic BP residue is positioned within the double helix on the 3′-side of the modified adenine residue. However, in a duplex in which all of the bases are complementary to one another, conformational heterogeneity precluded structural characterization of this adduct. The solution structures of the 10*R*-(−) *trans-anti*-[BP]-dA adduct have been obtained in both normally paired duplexes (*27*) and in a duplex in which a guanine is mismatched to the modified adenine (*28*). In all these cases with 10*R* adduct
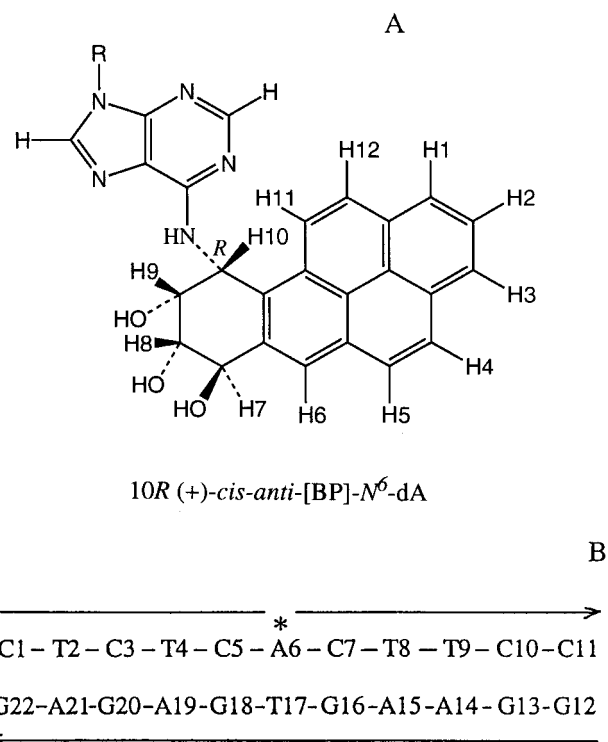

A

10*R* (+)-*cis-anti*-[BP]-N6-dA

B

FIGURE 1: (A) The chemical formula of 10*R*-(+)-*cis-anti*-[BP]-N6-dA. (B) The sequence of the (+)-*cis-anti*-[BP]dA·dT 11-mer duplex.

stereochemistry, the aromatic BP residue is positioned on the 5′-side of the modified adenine base (*27*), as in the 1R-(+)-*trans-anti*-[BPh]dA adduct (*23*).

We focus in the present study on the solution structure of a 10*R*-(+)-*cis-anti*-[BP]dA adduct (Figure 1A) in an 11-mer duplex with the normal partner base dT opposite the lesion (Figure 1B). This study is of interest for several reasons. In the case of the *anti*-[BP]dG adducts, there is striking difference in the conformations of the minor groove (+)-*trans-anti*- and (−)-*trans-anti*-[BP]dG (*29−30*) and the intercalative, base-displaced conformations of the steroisomeric (+)-*cis-anti*- and (−)-*cis-anti*-[BP]dG (*31−32*) lesions. Since the conformations of the 10*S*-(+)-*trans-anti*-[BP]dA are known to be intercalative without base displacement (*25−26*), it is of interest to compare this structure to the one derived from the 10*R*-(+)-*cis-anti*-[BP]dA adduct.

In the present research, a combined NMR-computational study including intensity based refinement on the (+)-*cis-anti*-[BP]dA adduct positioned opposite dT in an 11-mer duplex reveals that the pyrenyl moiety intercalates toward the 5′-side of the [BP]dA6 lesion site without disrupting the flanking Watson−Crick dC5·dG18 and [BP]dA6·dT17 base pairs. However, intercalation of the pyrenyl ring induces local distortion by causing buckling and propeller twisting of the Watson−Crick [BP]dA6·dT17 base pair.

MATERIALS AND METHODS

Oligonucleotide Synthesis. The deoxyoligonucleotides d(C−T−C−T−C−A−C−T−T−C−C) and d(G−G−A−A−G−T−G−A−G−A−G) were synthesized on an Applied Biosystems Model 392 DNA synthesizer and purified by reverse-phase HPLC methods.

Preparation of the (+)-cis-anti-[BP]dA·dT 11-mer Adducts. The oligonucleotide d(C−T−C−T−C−A−C−T−T−

C—C) (5 mM concentration) was directly reacted with racemic *anti*-BPDE in a 700 mM bis-tris propane buffer solution (pH 6.5) at ambient temperature. The (±)-*anti*-BPDE was dissolved in tetrahydrofuran (2 mg/mL), and 50 mL increments were added at 30 min intervals to the oligonucleotide solution with vigorous stirring until the final [BPDE]/DNA strand ratio was about 4−5. The fractions of modified oligonucleotides approached ∼10% under these conditions. The stereoisomeric reaction products were separated from one another, using reverse phase HPLC methods. The stereochemical properties of the adducts were determined by enzymatically digesting the modified oligonucleotides to the [BP]-N^6-dA mononucleoside levels, and their absolute configurations were determined by CD methods as described by Cheng et al. (*7*).

The purified (+)-*cis-anti*-[BP]-dA 11-mer d(C−T−C−T−C−A−C−T−T−C−C) strand (about 5 mg) was annealed to the complementary unmodified 11-mer d(G−G−A−A−G−T−G−A−G−A−G) strand by heating the solution to 70 °C; the stoichiometry was followed by monitoring single proton resonances in both strands. The NMR spectra of the (+)-*cis-anti*-[BP]dA·dT 11-mer duplex (4 mM in duplex) were recorded in a 0.1 M NaCl, 10 mM phosphate, 1 mM EDTA solution containing either D$_2$O or 90:10 H$_2$O/D$_2$O (v/v). All NMR spectra were obtained at pH 7.0.

NMR Experiments: All NMR spectra were recorded on Varian Unity plus 600 and 500 MHz NMR spectrometers. A combination of through-space nuclear Overhauser effect (NOESY) and through bond correlated (COSY and TOCSY) two-dimensional spectra were recorded in the States-TPPI mode (*33*) on approximately 5 mg of (+)-*cis-anti*-[BP]dA·dT 11-mer duplex in 0.5 mL aqueous buffer (100 mM NaCl, 10 mM phosphate, pH 7.0) solution at 25 °C and analyzed to assign the carcinogen and nucleic acid protons. The NOESY spectrum (150 ms mixing time) of the adduct duplex in H$_2$O buffer at 1 °C was collected using a jump-return pulse for solvent suppression. NOESY spectra (50, 90, 130, 170, and 200 ms mixing times) of the adduct duplex were collected to provide NOE build-up data on the adduct duplex in D$_2$O buffer at 25 °C with a relaxation delay of 2.5 s. The through-bond TOCSY data sets on the adduct duplex in D$_2$O buffer were recorded at spin lock times of 40 and 80 ms at 25 °C.

The indirect proton-phosphorus correlation spectrum was recorded on the (+)-*cis-anti*-[BP]dA·dT 11-mer duplex in D$_2$O at 25 °C using the pulse sequence described previously (*34*). The phosphorus spectra were referenced relative to external 10% trimethyl phosphate (TMP).

The proton−proton vicinal coupling constants among sugar protons were analyzed from phase-sensitive COSY data to qualitatively distinguish between the C3′-*endo* and C2′-*endo* family of sugar puckers (reviewed in *35*).

Structure Calculations. The structure calculations on the (+)-*cis-anti*-[BP]dA·dT 11-mer duplex were undertaken in two stages. The first step involves distance-restrained molecular mechanics calculations in torsion angle space using the DUPLEX program (*36*). The resulting energy minimized DUPLEX-based structure of the adduct duplex was next subjected to intensity-restrained relaxation-matrix-refinement computations to take into account the effect of spin diffusion.

Distance-Restrained Molecular Mechanics Computations. Minimized potential energy calculations were carried out

with DUPLEX, a molecular mechanics program for nucleic acids that performs potential energy minimizations in the reduced variable domain of torsion angle space (*36*). DUPLEX uses a potential set similar to the one developed by Olson and co-workers for nucleic acids (*37*). The geometry and linkage site of the (+)-*cis-anti*-[BP]dA adduct to adenine N^6 is the same as that of the (+)-*cis-anti*-[BP]dG adduct to guanine N^2 (*31*), including the benzylic ring conformation with pseudoequatorial orientation of the H7, H8, and H10 hydrogens and the pseudoaxial orientation of H9 (*7*). Force field parameters are also the same except that a new partial charge set, compatible with partial charges in DUPLEX (*36*), was computed with the CNDO method. The DUPLEX computational protocol on the (+)-*cis-anti*-[BP]-dA·dT 11-mer duplex is similar to that reported previously in our study of the (+)-*trans-anti*-[BPh]dA·dT 11-mer duplex (*23*). These DUPLEX calculations were carried out at the NSF San Diego Supercomputing Center and the DOE National Energy Research Supercomputing Center.

The calculation of interproton distance bounds using volume build-up of NOE cross-peaks was based on the two-spin approximation using the dT(NH3)−dA(H2) fixed distance of 2.92 Å for the NOESY data set in H$_2$O and the dC(H5)−dC(H6) fixed distance of 2.45 Å for the NOESY data sets in D$_2$O solution. The upper and lower bound ranges on the estimated interproton distances for nonexchangeable protons (based on a two spin approximation) were determined based on the resolution of the cross-peaks in the two-dimensional contour plots and the quality of the NOE build-up plots.

Relaxation Matrix Refinement. The energy minimized structure exhibiting the best goodness-of-fit indices following the completion of the first stage distance-restrained DUPLEX molecular mechanics calculations was used as the starting point for the second stage of intensity-restrained relaxation matrix refinement calculations using *X-PLOR* (*38*). In this second stage, we performed molecular dynamics/simulated annealing calculations guided by the combination of the experimental NOE intensities and NOE-based distances. The pseudoenergy function included two types of restraints: (1) intensity restraints for nonexchangeable protons were imposed as square-well potentials with an exponent of 2 in the penalty function, an isotropic correlation time of 5 ns, anisotropic bounds estimates of 10%, and a force constant of 50 kcal/mol·Å^2, (2) the distance restraints for nonexchangeable protons were retained through our protocol as square-well potentials with uniform 20% estimation of errors and a 30 kcal/mol·Å^2 force constant. A 4.5 Å cutoff was imposed for computing relaxation pathways and the dynamics was carried out with a tolerance of 0.03 Å.

The relaxation matrix was set up for the nonexchangeable protons with the exchangeable imino, amino, and hydroxyl protons exchanged for deuterons. A total of 1360 nonexchangeable intensity restraints (272 intensities per mixing time at 60ms, 90ms, 130ms, 170ms, and 200ms) from the NOESY data sets in D$_2$O and 272 nonexchangeable distance restraints were included in the calculations. Dihedral angle restraints (corresponding to B-DNA) were included with a very low weight of 5 kcal rad^{-2} and restricted to residues that are two pairs away in either direction from the [BP]dA lesion site.
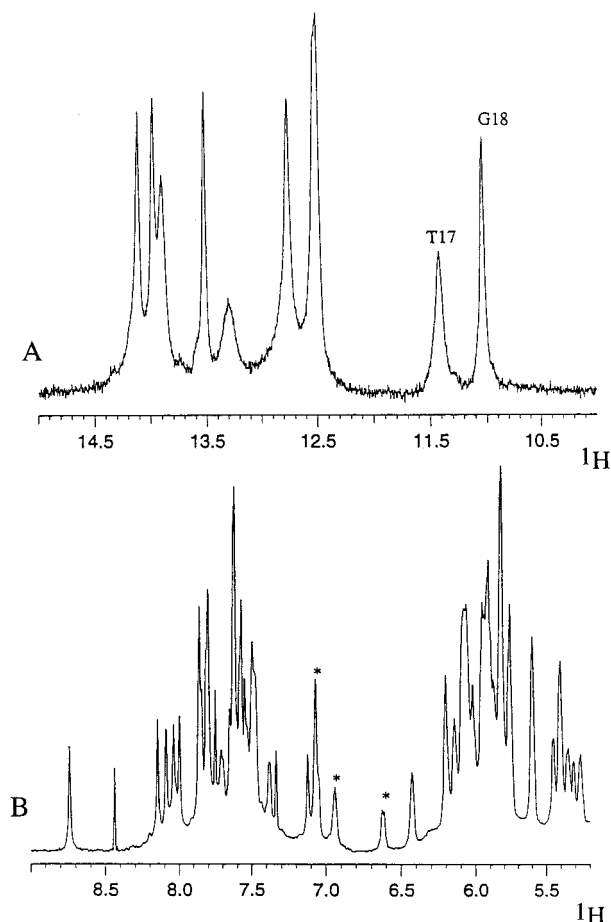
FIGURE 2: Proton spectra of the (+)-*cis-anti*-[BP]dA·dT 11-mer duplex. (A) Imino proton spectrum (10.0–15.0 ppm) in H_2O buffer at 1 °C and (B) nonexchangeable proton spectrum (5.2–9.0 ppm) in D_2O buffer at 25 °C. The buffer was 0.1 M NaCl, 10 mM phosphate, 0.1 mM EDTA, at pH 7.0. The imino proton assignments of dT17 and dG18 are shown over the resonances in (A). Several BP protons are indicated by asterisks in (B).

Six-intensity-refined computations were undertaken starting from the DUPLEX-based structure of the adduct duplex. During each of these computations, the starting structure was heated to 1000 °K through the assignment of an arbitrary Maxwell−Boltzmann velocity distribution corresponding to a temperature of 1000 °K. Then, after 2.4 ps dynamics evolution at that temperature, the system was gradually cooled to 300 °K during 7.2 ps with the "heat bath" method and equilibrated at 300 °K for 2.4 ps. After equilibration, the coordinates were subjected to energy minimization to a gradient of 0.1 kcal mol^{-1} Å^{-1}.

RESULTS

Exchangeable Protons. The exchangeable proton NMR spectrum (10.0 to 14.5 ppm) of the (+)-*cis-anti*-[BP]dA·dT 11-mer duplex in H_2O buffer solution, pH 7.0 at 1 °C is characterized by imino resonances dispersed between 12.5 and 14.0 ppm and two upfield shifted imino resonances at 11.41 and 11.04 ppm (Figure 2A). These imino protons have been assigned following analysis of NOE connenctivities between imino protons on adjacent base pairs in the NOESY (150 ms mixing time) spectrum of the adduct duplex in H_2O buffer at 1 °C (Figure 3B). Such connectivities between adjacent imino protons can be traced from dT2 at one end
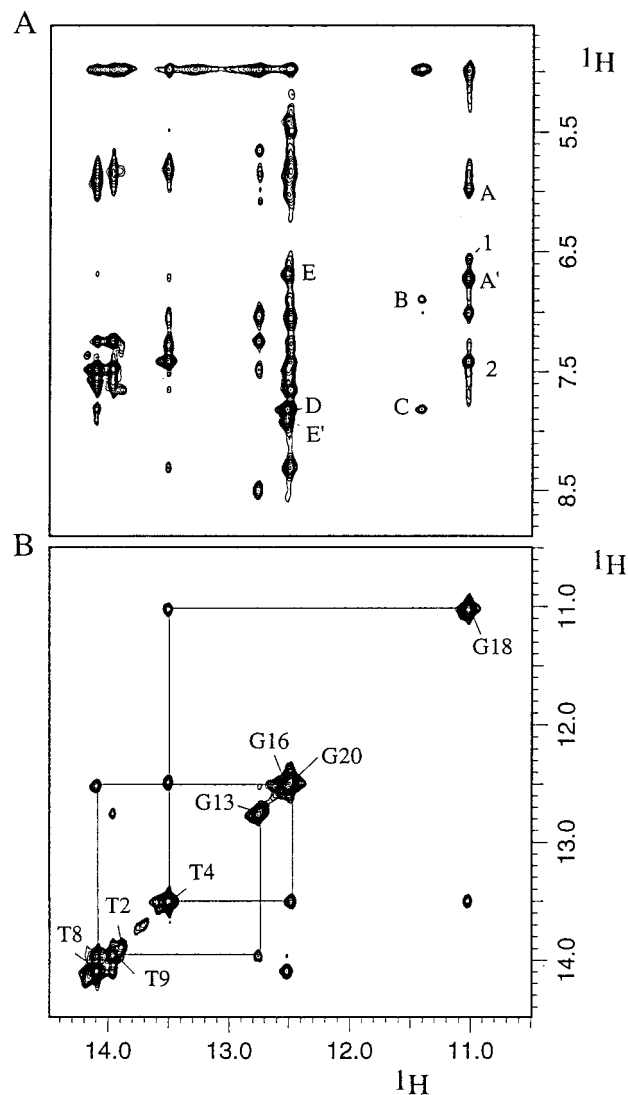

FIGURE 3: Expanded NOESY (150 ms mixing time) contour plots of the (+)-*cis-anti*-[BP]dA·dT 11-mer duplex in H_2O buffer at 1 °C. (A) Expanded plot of the NOE connectivities between the imino protons (10.5–14.5 ppm) and the base and amino protons (4.5–9.0 ppm) region. The NOE cross-peaks involving the imino protons are labeled in the figure as follows: A,A′, G18(NH1)−C5(NH$_2$-4b,e); B, T17(NH3)−[BP]A6(NH-2); C, T17(NH3)-[BP]A6(H2); D, G16(NH1)-[BP]A6(H2); F,F′, G16(NH1)−C7(NH$_2$-4b,e). The intermolecular NOE cross-peaks 1 to 2 are assigned as follows: 1, G18(NH1)−BP(H11) and 2, G18(NH1)−BP(H12). (B) Expanded plot of the NOE connectivities within the symmetrical imino proton (10.5–14.5 ppm) region. The lines trace the NOE connectivities between adjacent imino protons along the helix. We do not observe a cross-peak for the imino proton of dT17 along the diagonal.

to dG13 at the other end of the helix, except for a break at the dG16−dT17−dG18 step in the adduct duplex (Figure 3B).

The NOE connectivities between the imino protons (10.5–14.5 ppm) and the base and amino protons (4.5–9.0 ppm) in an expanded NOESY (150 ms mixing time) contour plot of the [BP]dA·dT 11-mer duplex in H_2O buffer at 1 °C is plotted in Figure 3A. The observed NOE patterns establish Watson−Crick base pairing at all dA·dT pairs (NOE between thymine imino to adenine H2 protons) and at all dG·dC pairs (NOE between guanine imino to cytosine amino and H5 protons). The upfield shifted imino proton at 11.04 ppm is assigned to dG18 based on NOEs to the amino protons of

Table 1: Proton Chemical Shifts of the
d(T4−C5−[BP]A6−C7−T8)·d(A15−G16−T17−G18−A19)
Segment of the (+)-*cis-anti*-[BP]dA·dT 11-mer Duplex in Aqueous
Buffer

A. Nucleic Acid Exchangeable Proton Chemical Shifts (ppm) at 1 °C

	G(NH1)/T(NH3)	C(NH$_2$-4)
dT4·dA19	13.52	
dC5·dG18	11.04	6.72[a], 5.98[b]
[BP]dA6·dT17	11.41	
dC7·dG16	12.53	7.93[a], 6.68[b]
dT8·dA15	14.11	

B. Nucleic Acid Nonexchangeable
Proton Chemical Shifts (ppm) at 25 °C

	H8/H6	H2/H5/CH$_3$	H1′	H2′,H2″	H3′	H4′	^{31}P[c]
dT4	7.12	1.41	5.82	1.71,2.00	4.74	4.04	−4.28
dC5	7.50	5.09	5.93	2.57,2.48	5.06	4.27	−3.30
[BP]dA6	8.74	7.86	6.42	2.82,2.93	5.12	4.54	−4.15
dC7	7.61	5.44	6.05	2.27,2.47	4.87	4.31	−3.90
dT8	7.49	1.62	6.08	2.23,2.59	4.87	4.22	−4.36
dA15	7.87	7.55	5.82	2.34,2.55	4.92	4.30	−4.24
dG16	7.07		5.40	1.71,1.88	4.64	3.83	−4.28
dT17	5.90	0.04	5.28	1.66,1.94	4.60	3.83	−2.33
dG18	7.80		4.88	2.62,2.67	4.79	3.92	−3.70
dA19	8.09	7.49	5.82	2.67,2.76	5.00	4.37	−4.12

C. Benzopyrenyl Proton Chemical Shifts (ppm) at 25 °C

H1	H2	H3	H4	H5	H6	H7	H8	H9	H10	H11	H12
7.07	6.94	7.38	7.70	7.80	8.04	5.31	4.21	4.21	5.92	6.62	7.05

[a] Hydrogen-bonded amino proton. [b] Exposed amino proton; na, Not
available. [c] ^{31}P chemical shift corresponds to residue (*n*) for the (*n*)-
^{31}P-(*n*+1) step.

dC5 (peaks A and A′, Figure 3A) and the upfield shifted
imino proton at 11.41 ppm is assigned to dT17 based on
weak NOEs to the H2 (peak C, Figure 3A) and the amino
proton (peak B, Figure 3A) of [BP]dA6 in the adduct duplex.
The latter NOEs establish formation of a Watson−Crick [BP]-
dA6·dT17 base pair in the adduct duplex. The imino proton
of dT17 is broad in the exchangeable proton spectrum at
pH 7.0 and 1 °C (Figure 2A) and cannot be observed as a
peak along the diagonal of the 150 ms mixing time NOESY
contour plot at pH 7.0 and 1 °C (Figure 3B), suggesting that
its exchange rate is faster than a normal dA·dT base pair in
the adduct duplex. Such an increased rate of exchange for
the imino proton of dT17 could account for the weak NOEs
(peaks B and C, Figure 3A) observed experimentally across
the [BP]dA6·dT17 base pair in the adduct duplex.

The exchangeable imino and amino proton chemical shifts
for the central d(T4−C5−[BP]A6−C7−T8)·d(A15−G16−
T17−G18−A19) segment of the (+)-*cis-anti*-[BP]dA·dT 11-
mer duplex at 1 °C are listed in Table 1 and for the entire
adduct duplex in Supplementary Table S1 (Supporting
Information).

Nonexchangeable Nucleic Acid Protons. We observe
narrow and partially resolved base and sugar H1′ nonex-
changeable proton resonances in the 5.2−9.0 ppm spectral
region of the (+)-*cis-anti*-[BP]dA·dT 11-mer duplex in D$_2$O
buffer, pH 7.0 at 25 °C (Figure 1B). Nonexchangeable proton
assignments are based on an analysis of through space
NOESY (50 and 300 ms mixing times) data sets and through
bond COSY and TOCSY (40 and 80 ms spin lock times)
data sets at 25 °C using methods described in the literature
(reviewed in *35, 39*).

The expanded NOESY (300 ms mixing time) contour plot
establishing sequential connectivities between the base
protons (5.6−8.8 ppm) and the sugar H1′ and cytosine H5
protons (4.7−6.5 ppm) of the (+)-*cis-anti*-[BP]dA·dT 11-
mer duplex in D$_2$O buffer, pH 7.0 at 25 °C is plotted in
Figure 4A. The base to sugar H1′ proton NOE connectivities
are traced from dT4 to dT8 along the modified strand (solid
line, Figure 4A) and from dA15 to dA19 along the
complementary strand (dashed line, Figure 4A) in the adduct
duplex. The NOE connectivity is missing between the dT17
(H1′) proton and the G18(H8) proton (boxed region, Figure
4A) due to a break in the connectivity at the dT17−dG18
step in the adduct duplex. These base and sugar H1′ proton
assignments have been confirmed by cross-checks in other
regions of the NOESY plot, as well as from COSY and
TOCSY plots, which yield, in addition, a complete set of
sugar H2′, H2″, H3′, and H4′ proton assignments in the
adduct duplex. The chemical shifts of the nonexchangeable
nucleic acid protons for the d(T4−C5−[BP]A6−C7−T8)·
d(A15−G16−T17−G18−A19) segment of the (+)-*cis-anti*-
[BP]dA·dT 11-mer duplex at 25 °C are listed in Table 1B
and for the entire adduct duplex in Supplementary Table S2
(Supporting Information). The benzo[*a*]pyrenyl protons were
assigned from an analysis of the through-space NOE patterns
and through-bond coupling connectivities in the adduct
duplex with their chemical shifts 25 °C listed in Table 1C.

We observe large upfield chemical shifts for the H6 (5.90
ppm), H1′ (5.28 ppm), and CH$_3$ (0.04 pm) protons of dT17
and the H1′ proton of dG18 (4.88 ppm), while large
downfield shifts are observed for the H8 (8.74 ppm) and
H1′ (6.42 ppm) protons of [BP]dA6 in the adduct duplex
(Table 1B). The aromatic pyrenyl protons of the BP ring in
the adduct duplex resonate between 6.5 and 8.0 ppm (Table
1C), which are upfield of the 8.0−8.5 ppm range observed
for pyrenyl rings positioned in the groove of the duplex (*29−
30*).

Phosphorus Spectra: The proton-decoupled-phosphorus
spectrum of the (+)-*cis-anti*-[BP]dA·dT 11-mer duplex has
been recorded in D$_2$O buffer at 25 °C. The phosphorus
resonances are dispersed over an ~2.0 ppm range with three
resonances shifted to the low field of the −3.9 to −4.5 ppm
spectral region. The phosphorus resonances have been
assigned through correlation to the 5′-linked H3′ protons and
the 3′-linked H4′ and H5′ and 5″ protons in the proton
detected phosphorus-proton heteronuclear correlation spec-
trum of the adduct duplex at 25 °C as shown in Figure 4B.
The phosphorus chemical shifts in the adduct duplex at 25
°C are listed in Table 1B. The downfield-shifted phosphorus
resonances are assigned to the dC5−[BP]dA6 (−3.30 ppm),
dT17−dG18 (−2.33), and dG18−dA19 (−3.70 ppm) steps
in the adduct duplex (Figure 4B).

Structural Restraints. A set of intermolecular BP-DNA
NOE cross-peaks have been identified in the NOESY spectra
of the (+)-*cis-anti*-[BP]dA·dT 11-mer duplex with several
of these labeled by numbers in the expanded NOESY plots
of the exchangeable protons in H$_2$O solution (Figure 3) and
nonexchangeable protons in D$_2$O solution (Figures 4A).
These carcinogen−DNA NOEs in the adduct duplex are
listed in Table 2 with the majority of the intermolecular
NOEs observed between the pyrenyl protons of BP and the
base and sugar protons of dT17 located on the unmodified
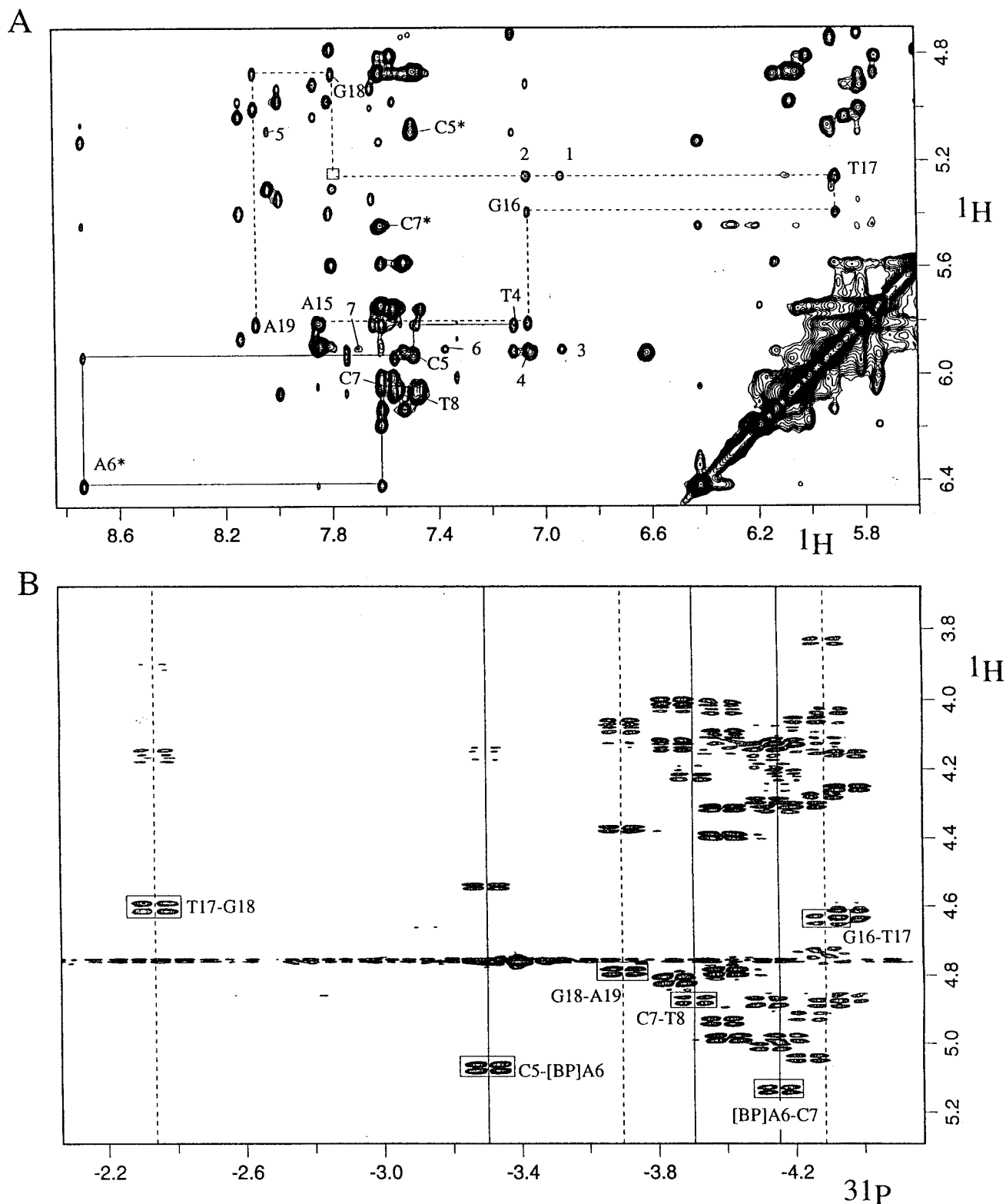strand opposite [BP]dA6 in the adduct duplex (Table 2).

A

B

FIGURE 4: (A) An expanded NOESY (300 ms mixing time) contour plot of the (+)-*cis-anti*-[BP]dA·dT 11-mer duplex in D₂O buffer at 25 °C establishing distance connectivities between the base protons (5.6−8.8 ppm) and the sugar H1′ and 2′-deoxycytidine H5 protons (4.7−6.5 ppm). The NOE connectivities between the base and their own and 5′-flanking sugar H1′ protons from dT4 to dT8 on the modified strand are shown by solid lines and from dA15 to dA19 on the unmodified partner strand are shown by dashed lines. The assignments label the base to their own sugar H1′ NOEs, while the deoxycytidine H6−H5 NOEs are designated by asterisks. The carcinogen-DNA NOE cross-peaks 1−7 are assigned as follows: 1, T17(H1′)−BP(H2); 2, T17(H1′)−BP(H1); 3, T17(H6)−BP(H2); 4, T17(H6)−BP(H1); 5, C5(H5)−BP(H6); 6, T17(H6)−BP(H3); 7, T17(H6)−BP(H4). (B) An expanded contour-plot of the proton-detected phosphorus-proton heteronuclear correlation experiment on the (+)-*cis-anti*-[BP]dA·dT 11-mer duplex in D₂O buffer at 25 °C. The phosphorus assignments are listed for steps centered about the lesion site. The correlation cross-peaks between the phosphorus and its 5′-flanking sugar H3′ protons are boxed.

Table 2: Intermolecular NOEs between Benzo[a]pyrene-dA6 Protons and DNA Protons in the (+)-*cis-anti*-[BP]dA·dT 11-mer Duplex

BP protons	DNA protons with NOEs to BP protons
BP(H1)	dT17(H6, H1′, H2″),
BP(H2)	dT17(H6, H1′, H2′, H2″, H3′)
BP(H3)	dT17(H6, H2′, H2″, CH$_3$)
BP(H4)	dT17(H6, CH$_3$)
BP(H5)	dT17(CH$_3$)
BP(H6)	dC5(H5), dT17(CH$_3$)
BP(H11)	dC5(H6), [BP]dA6(H2), dT17(NH), dG18(NH)
BP(H12)	dT17(NH), dG18(NH)
[BP]dA6(H2)	dG16(NH)
[BP]dA6(H8)	dC5(H1′)

Distance-Restrained Molecular Mechanics Computations: The search strategy employed began with a B-DNA (*40*) central d(T4−C5−[BP]A6−C7−T8)·d(A15−G16−T17−G18−A19) base pair segment of the (+)-*cis-anti*-[BP]-dA·dT 11-mer duplex. The molecular mechanics based DUPLEX computations were guided by the intramolecular DNA and intermolecular BP-DNA restraints for this segment of the adduct duplex. The BP-DNA orientation space was searched with 16 energy minimization trials in which the linkage torsion angles α′ ([BP]dA(N^1)−[BP]dA(C^6)−[BP]-dA(N^6)−[BP]dA(C^{10})) and β′ ([BP]dA(C^6)−[BP]dA(N^6)−[BP]dA(C^{10})−[BP]dA(C^9)) were each started at 0°, 90°, 180°, 270° in all combinations. In these trials, the DUPLEX hydrogen-bond penalty function (*36*) for Watson−Crick base pairing was utilized at all base pairs, since the NMR data indicated that these hydrogen bonds were present.

Four out of the 16 computed structures exhibited good fit to the NMR data and had low energies. These four structures are shown in Supplementary Figure S1 (Supporting Information) and their energies and goodness-of-fit indices are listed in Table S3 (Supporting Information). The structure with lowest energy and goodness-of-fit indices (Table S3) was embedded into an energy minimized B-form 11-mer and reminimized with all restraints. Subsequently, the hydrogen bond penalty function and the distance restraints were released with energy minimization in one step, yielding the unrestrained structure that was employed for subsequent relaxation matrix refinement computations.

Relaxation Matrix Refinement. The protocol for relaxation matrix refinement undertaken at 1000 °K on the entire (+)-*cis-anti*-[BP]dA·dT 11-mer duplex is outlined in the Materials and Methods section. An ensemble of six intensity refined structures (derived from the starting DUPLEX-based structure) demonstrated an improved correspondence with experimental intensity and distance restraint data sets compared to the starting structure obtained from the first stage DUPLEX calculations. The number of NOE distances violated by >0.2 Å decreased from 30 to 4 (with only three violations in the central 5-mer d(T4−C5−[BP]A6−C7−T8)·d(A15−G16−T17−G18−A19) segment with respect to different structures in the ensemble), and the NMR *R*-factor ($R_{1/6}$) improved from an initial value 6.8 to 2.4%. The experimental distance bounds of the [BP]dA·dT 11-mer duplex are compared with those obtained after relaxation matrix refinement in Supplementary Table S4 (Supporting Information).

The pairwise rmsd values among the six intensity refined structures in the set is 1.59 ± 0.42 Å for all heavy atoms,

Table 3: NMR Refinement Statistics for the (+)-*cis-anti* [BP]dA·dT 11-mer Duplex

NMR distance restraints	
entire 11-mer adduct duplex	272
central 5-mer region[a]	148
carcinogen-DNA restraints	19
NMR intensity restraints	
entire 11-mer adduct duplex	1360 (5 mixing times)
central 5-mer region[a]	740 (5 mixing times)
structure statistics	
NMR *R*-factor ($R_{1/6}$)	0.024 ± 0.001
rmsd of NOE violations	0.047 ± 0.005
number of NOE violations >0.2 Å in the entire adduct duplex	3.8 ± 1.2
number of NOE violations >0.2 Å in the central 5-mer region[a]	3.0 ± 1.1
deviations from the ideal geometry	
bond length (Å)	0.012 ± 0.001
bond angle (deg)	3.25 ± 0.04
impropers (deg)	0.32 ± 0.05
pairwise rmsd (Å) among the six intensity refined structures (heavy atoms only)	
the entire 11-mer adduct duplex	1.59 ± 0.42
the central 5-mer region[a]	1.18 ± 0.25
the central 5-mer region without backbone[a]	0.79 ± 0.18

[a] The d(T4−C5−[BP]A6−C7−T8)·d(A15−G16−T17−G18−A19) segment.

1.18 ± 0.25 Å for the heavy atoms of the central d(T4−C5−[BP]A6−C7−T8)·d(A15−G16−T17−G18−A19) 5-mer segment and 0.79 ± 0.18 Å for the heavy atoms of 5-mer excluding backbone (see Table 3). The structures exhibit good stereochemistry with reasonable rmsd values for bond length, bond angle, and improper dihedral angle violations (Table 3).

A view of the six superpositioned strucutres of the d(T4−C5−[BP]A6−C7−T8)·d(A15−G16−T17−G18−A19) segment of the (+)-*cis-anti*-[BP]dA·dT 11-mer duplex is plotted in Figure 5A. The corresponding view looking down the helix axis of the central d(C5−[BP]A6−C7)·d(G16−T17−G18) segment of the adduct duplex is plotted in Figure 5B.

Solution Structures. The corresponding view of the d(T4−C5−[BP]A6−C7−T8)·d(A15−G16−T17−G18−A19) segment in one representative intensity refined structure of the (+)-*cis-anti*-[BP]dA·dT 11-mer duplex is plotted in Figure 6A. The covalently linked BP ring intercalates into the helix between the dC5·dG18 and [BP]dA6·dT17 base pairs and this is achieved through considerable buckling and propeller-twisting of the [BP]dA6·dT17 base pair (Figure 6A).

A view looking down the helix axis of the central d(C5−[BP]A6)·d(G16−T17−G18) segment in one representative intensity refined structure of the (+)-*cis-anti*-[BP]dA·dT 11-mer duplex is shown in Figure 6B. This view emphasizes the overlap geometry between the pyrenyl ring system and the flanking dC5·dG18 and [BP]dA6·dT17 base pairs. The pyrenyl ring overlaps with the flanking base rings of dC5 on the modified strand and dT17 and dG18 on the unmodified strand of the adduct duplex (Figure 6B).

The carcinogen-base linkage site torsion angles for the [BP]dA6 residue adopt values of α′ = 160° ± 10° and β′ = 107° ± 14° respectively, together with a normal antiglycosidic torsion angle of χ = 258° ± 6° among the six intensity refined solution structures of the adduct duplex. The sugar pseudorotation parameters and glycosidic torsion angles for the d(T4−C5−[BP]A6−C7−T8)·d(A15−G16−T17−G18−
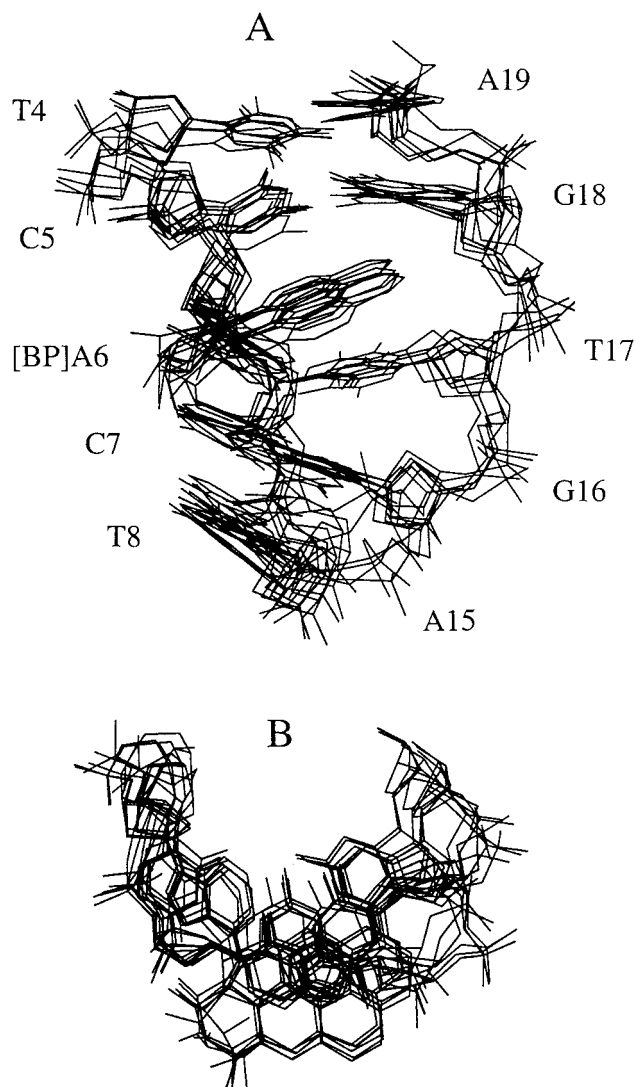
FIGURE 5: (A) The superposition of the d(T4−C5−[BP]A6−C7−T8)·d(A15−G16−T17−G18−A19) segments of the six intensity refined structures of the (+)-*cis-anti*-[BP]dA·dT 11-mer duplex. View looking into the major groove and normal to the helix axis. (B) The superposition of the d(C5−[BP]A6−C7)·d(G16−T17−G18) of the six intensity refined structures of the (+)-*cis-anti*-[BP]-dA·dT 11-mer duplex. View looking down the helix axis.

A19) segment of the intensity refined structures of the (+)-*cis-anti*-[BP]dA·dT 11-mer duplex are listed in Supplementary Table S5 (Supporting Information). The majority of these angles are within or near ranges observed in B-DNA crystals, with several in less common domains associated with the accommodation of the intercalated pyrenyl ring into the helix.

A stereoview of one representative intensity refined structure of the entire (+)-*cis-anti*-[BP]dA·dT 11-mer duplex is shown in Figure 7.

DISCUSSION

Intercalation Site. In classical intercalation, the polycyclic aromatic ligands are assumed to be inserted between adjacent base pairs with their planes approximately parallel to one other. In addition, the duplex is stretched and unwound in order to accommodate the intercalated molecule. In the case of the 10*S* and 10*R* covalent [BP]dA adducts in double-stranded DNA, the conformations resemble those of classical intercalation complexes, but there are some important
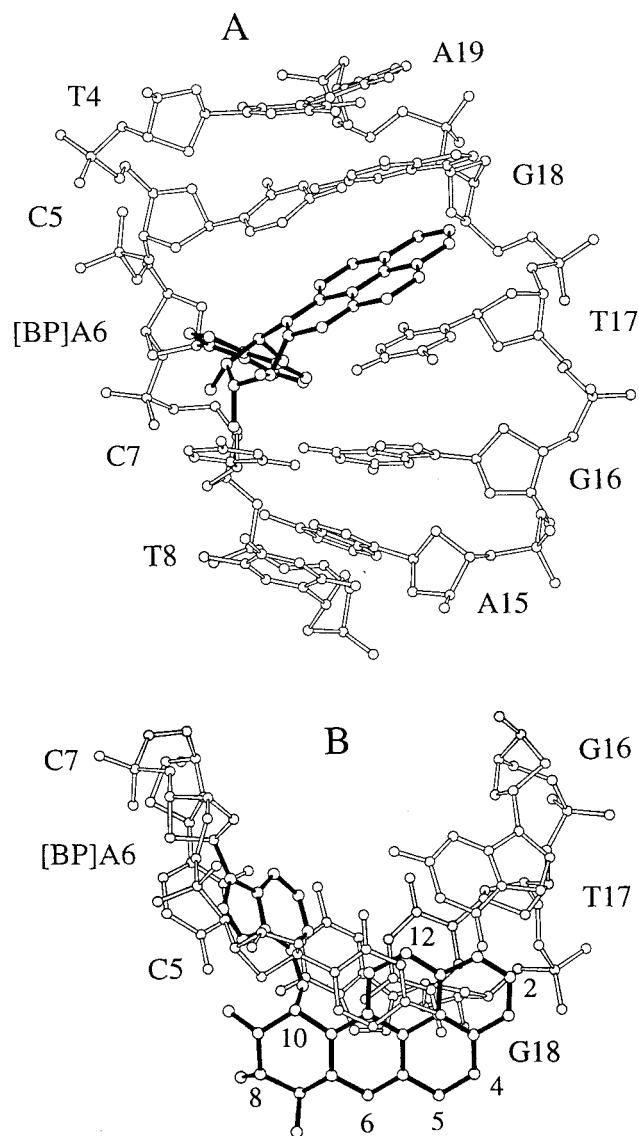
FIGURE 6: A representative intensity refined structure of the (+)-*cis-anti*-[BP]dA·dT 11-mer duplex. (A) View looking into the major groove and normal to the helix axis of the d(T4−C5−[BP]A6−C7−T8)·d(A15−G16−T17−G18−A19) segment. The BP ring system and attached adenine are shown in darkened bonds with the benzo[*a*]pyrenyl ring intercalated between dC5·dG18 and [BP]-dA6·dT17 base pairs. (B) View looking down the helix axis for the d(C5−[BP]A6−C7)·(d(G16−T17−G18) segment in the intensity refined structure of the (+)-*cis-anti*-[BP]dA·dT 11-mer duplex. Figures were prepared using Molscript V1.1 (*47*).

differences, including buckling and propeller-twisting of the modified base pair.

The pyrenyl ring of [BP]dA6 intercalates into the DNA duplex toward the 5′-end of the modified strand, between the dC5·dG18, and modified [BP]dA6·dT17 base pairs, without disruption of the Watson−Crick alignments of either pair (Figure 6A). However, the [BP]dA6·dT17 base pair buckles and propeller twists significantly in order to accommodate the intercalated pyrenyl ring without disruption of the base pair alignment. We compute values of −35.4° for buckle and 26.0° for propeller-twisting of the [BP]dA6·dT17 base pair following analysis of helical parameters (*41*). In addition, the helix both unwinds and stretches locally at the pyrenyl intercalation site with a twist angle of 27.2° and a helical rise of 7.8 Å between the dC5·dG18 and the [BP]-dA6·dT17 pairs in the adduct duplex.
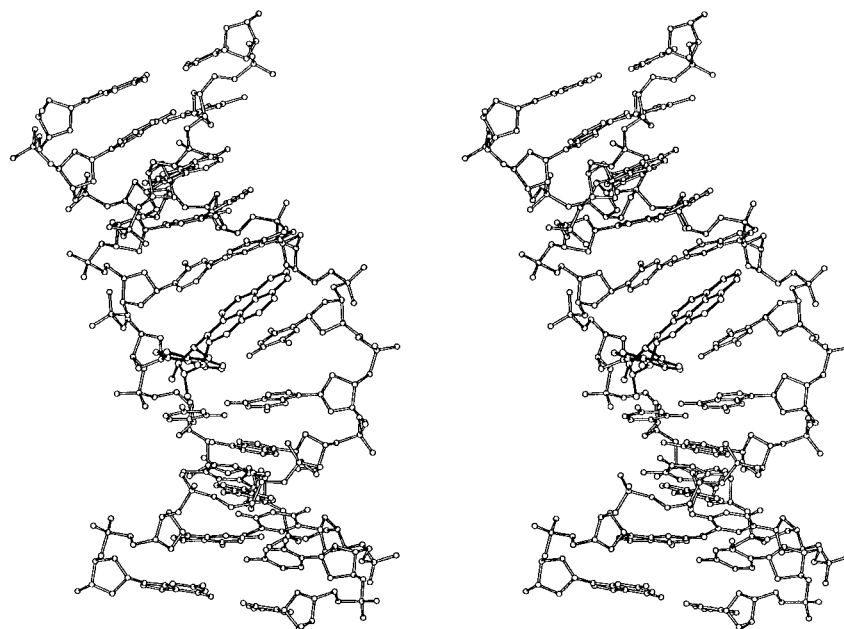
FIGURE 7: A view normal to the helix axis of the representative intensity refined structure of the entire (+)-*cis-anti*-[BP]dA·dT 11-mer duplex. Figure was prepared using Molscript V1.1 (*47*).

The buckling and propeller-twisting of the [BP]dA6·dT17 base pair directs the H2 proton containing edge of [BP]dA6 toward the dC7·dG16 base pair (Figure 6A) consistent with the observation of a strong NOE between the adenine H2 proton of [BP]dA6 and the imino proton of dG16 (peak D, Figure 3A) in the adduct duplex (Table S4). The buckling and propeller-twisting of the [BP]dA6·dT17 base pair probably accounts for the faster exchange of the imino proton dT17 as manifested in its broader line width in one-dimensional spectra (Figure 2A) and the absence of a diagonal cross-peak at its chemical shift in the expanded NOESY contour plot (Figure 3B) of the adduct duplex.

Both the NOE and chemical shift patterns support intercalation of the pyrenyl ring between dC5·dG18 and [BP]-dA6·dT17 base pairs in the adduct duplex. Such an alignment (Figure 6A) readily accounts for the break in the sequential NOE connectivity observed between the H1′ of dT17 and H8 of dG18 at the dT17−dG18 step (boxed region, Figure 4A) in the expanded NOESY contour plot of the adduct duplex. The intercalation of the pyrenyl ring between the dC5·dG18 and [BP]dA6·dT17 base pairs readily explains the observed upfield shifts of the aromatic pyrenyl ring protons from their unperturbed chemical shift range of 8.0−8.5 ppm to the 6.5−8.0 ppm range (Table 1C) in the (+)-*cis-anti*-[BP]dA·dT 11-mer duplex. It also explains the upfield shifts of the dT17 and dG18 imino protons (Figure 1A) of the [BP]dA6·dT17 and dC5·dG16 base pairs that flank the intercalation site. The intercalated pyrenyl ring extends toward the partner strand and stacks extensively with the dT17 and dG18 residues accounting for the obseved upfield shifts (Table 1) of the base (H6 and CH₃) and sugar (H1′) protons of dT17 and the sugar (H1′) proton of dG18 in the adduct duplex.

Benzylic Ring Conformation: The H7, H8, and H10 hydrogens are pseudoequatorial, and H9 is pseudoaxial in the intensity refined structures of the (+)-*cis-anti*-[BP]dA·dT 11-mer duplex, in line with the conformation observed for this adduct at the nucleoside level (*7*). This conformation

could not be independently verified from a coupling constant analysis because of an overlap of the benzylic H8 and H9 protons in the spectra of the adduct duplex. We are confident in the correctness of this benzylic ring pucker since, in our experience, incorrectly assumed benzylic ring puckers do not yield refined structures with low goodness-of-fit indices in DUPLEX calculations and low *R*-values in intensity refinement calculations.

Comparison with Structures of Other Adenine Adducts. In all the adenine adducts studied so far, which include [BPh]-dA (*23−24*) and [BP]dA (*25−28, 42*), the polycyclic ring systems are intercalatively inserted on the 5′ side in the case of *R* adduct stereochemistry, and on the 3′ side of the modified adenine residues in the case of *S* adduct stereochemistry. The present (+)-*cis-anti*-[BP]dA·dT 11-mer duplex, with 10*R* linkage stereochemistry, fits into this theme, since the BP residue is sandwiched between base pairs on the 5′ side of the modified dA6 residue. It should be noted, however, that the degree of buckling of the [BP]dA6·dT17 base pair in the (+)-*cis-anti*-[BP]dA·dT 11-mer duplex (present study) is more pronounced than what was reported previously for the (+)-*trans-anti*-[BPh]dA6·dT17 base pair in the (+)-*trans-anti*-[BPh]dA·dT 11-mer duplex (Figure 8A) (*23*).

Comparison with [BP]dG Adducts. In duplexes in which all of the bases are complementary to one another, the structural themes adopted by the 10*R*-(−)-trans- (*30*) and 10*R*-(+)-*cis*-[BP]dG adducts (*31*) are remarkably different from those adopted by the configurationally similar 10*R*-(−)-trans (*27*) and (+)-*cis*- (present study) [BP]dA adducts. In the (−)-*trans*-[BP]dG adduct, the aromatic BP ring system is positioned in the minor groove and is directed toward the 3′-end of the modified strand (*30*). In the (+)-*cis*-[BP]dG adduct on the other hand, the BP residue is intercalatively inserted into the double helix, and the modified guanine and partner cytosine bases are displaced into the minor and major grooves, respectively (base-displaced-intercalation, Figure 8B). A remarkable change in conformation is observed when
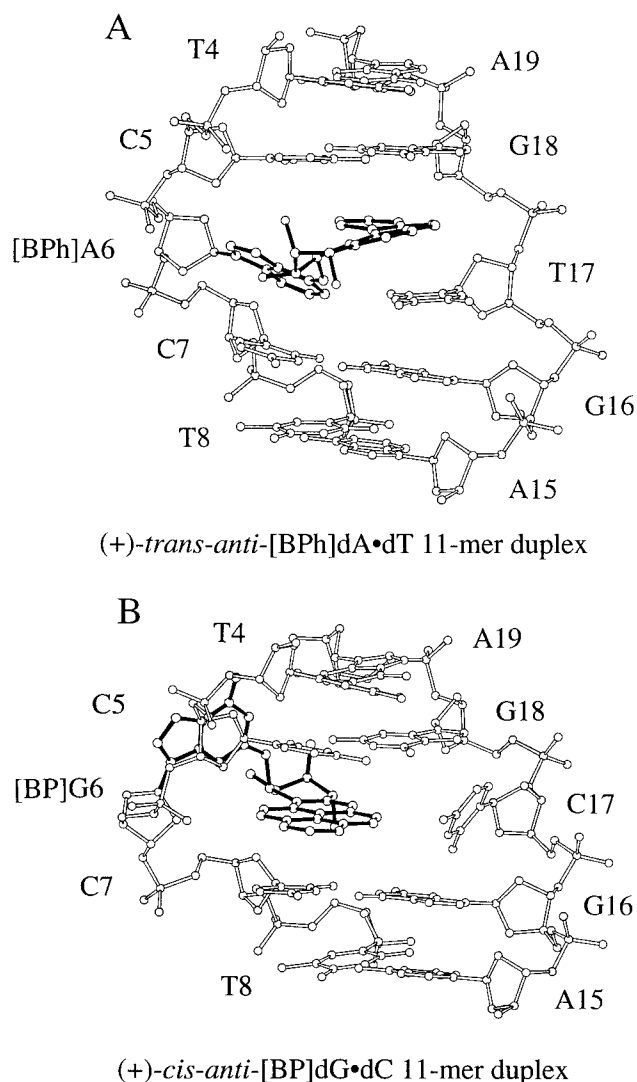
A

(+)-*trans-anti*-[BPh]dA•dT 11-mer duplex

B

(+)-*cis-anti*-[BP]dG•dC 11-mer duplex

FIGURE 8: Comparative views of the solution structures of (A) the d(T4−C5−[BPh]A6−C7−T8)·(d(A15−G16−T17−G18−A19) segment of the (+)-*trans-anti*-[BPh]dA·dT 11-mer duplex (*23*) and (B) the d(T4−C5−[BP]G6−C7−T8)·(d(A15−G16−C17−G18−A19) segment of the (+)-*cis-anti*-[BP]dG·dC 11-mer duplex (*31*).

the cytosine base on the partner strand, opposite to the (−)-*trans*-[BP]dG adduct, is deleted: the BP residue adopts an intercalative conformation with the modified guanine displaced into the minor groove in the "deletion duplex" (*43*). By contrast, both the 10*R*-(−)-trans- and (+)-*cis*-[BP]dA lesions are characterized by similar intercalative conformations with the BP ring system intercalatively inserted on the same (5′) side of the modified dA residue.

A key question is why do adenine adducts appear to universally adopt classical intercalation type structures, while guanine adducts do not? Classical intercalation would appear to afford the energetically least costly avenue for accommodating the hydrophobic BP aromatic ring system, since the modified base pairs are neither denatured nor unstacked, as in the base-displaced-intercalation structures. It appears that intercalation without base displacement is feasible in [BPh]dA (*23*−*24*) and [BP]dA (*28*) adducts with the benzylic ring of the carcinogens positioned in the sterically spacious major groove where considerable flexibility appears to be possible at the covalent tether linking the carcinogen to the N⁶-adenine position of the DNA. On the other hand, in the

case of the [BP]dG adducts, the benzylic ring of the carcinogen is positioned in the sterically crowded DNA minor groove. It is apparently energetically too costly to achieve the flexibility needed for classical intercalation without a disruption of the modified base pair for [BP]dG adducts in DNA. However, intercalation by base displacement, at the expense of Watson−Crick hydrogen bonding and destacking of the modified bases, is preferred in the case of the (+)-*cis-anti*-[BP]dA adduct in normal duplexes. These considerations may account for the fact that the (+)-*cis-anti*-[BP]dA adduct reported in this study adopts a nearly classical intercalation conformation, while the (+)-*cis-anti*-[BP]dG adduct adopts a base-displaced intercalative conformation (*31*).

Biological Implications. The mechanisms associated with the cellular processing of structurally isomeric adducts derived from the binding of different polycyclic aromatic hydrocarbon diol epoxides to DNA is of great current interest (reviewed in ref *22*). Carcinogen-modified DNA sequences can be removed prior to replication by nucleotide excision repair enzymes. It has recently been shown that the stereoisomeric *cis*- and *trans*-[BP]dG adducts are processed by human nucleotide excision repair proteins at remarkably different rates (*44*). Related information on the repair of [BP]-dA lesions is not yet available. These results suggest that adduct conformation can have profound consequences on the rates of removal of these lesions by the cellular repair proteins.

If not repaired, the modified sequences can adversely influence transcription and/or DNA replication. For example, *in vivo* replication studies of the (+)-*cis*-[BP]dA at position 2 of the *N-ras* codon 61 sequence has revealed that it causes A to G transition mutations at a frequency of 0.60% in repair-deficient *E. coli* cells, indicating that a C is inserted opposite the lesion during replication (*45*). In *in vitro* primer extension reactions using a template strand of 33 bases long with the same (+)-*cis*-[BP]dA adduct located at the sixth position from the 5′-end, a normal T is preferentially inserted opposite the lesion in the case of the polymerases Pol α, Pol β, the *Exo*⁺ Klenow fragment (*46*), and the HIV-1 transcriptase (*47*); however, in the case of Sequenase 2.0 and the *Exo*⁻ Klenow fragment, the bases C or A, respectively, are preferentially inserted (*46*), resulting in A to G or A to T mutations. These results suggest that the mutagenic specificity of the (+)-*cis*-[BP]dA adduct positioned in identical sequence contexts, depends on the polymerases and can vary significantly from one polymerase to the other. It is, therefore, difficult to speculate about the possible conformational characteristics that might be assumed by the (+)-*cis*-[BP]dA at the single strand-double strand junctions during replication.

One structural feature, observable in the duplexes containing (+)-*cis*-[BP]dA and similar adducts, appear to manifest itself in DNA replication. In *in vitro* replication studies with a variety of polymerases, all stereoisomeric [BP]dA adducts were shown to block primer extension at sites just before or opposite the modified dA residues. However, [BP]dA adducts with 10*S* absolute configuration at the [BP]dA linkage site, block extension just prior to the modified dA residue, while those with 10*R* stereochemistry allow for primer extension by one additional residue, by the insertion of a nucleotide opposite to the modified dA (*46*−*48*). *These differences*

are attributed to the orientations of the bulky BP residues either on the 3′-side of the modified dA (10*S*) or on the 5′-side (10*R*) of the modified dA residue. In the case of the 10*R*-(+)-*cis*-[BP]dA adducts, the orientation of the BP residue on the 5′-side allows for an easier insertion of a nucleotide opposite the modified dA than in the case of the 10*S* isomers where the adducts are positioned on the 3′-side (*46−48*). The observed adduct orientation on the 5′-side of the modified base in our (+)-*cis*-[BP]dA adduct, is consistent with the observed polymerase stop sites (*47,48*).

Coordinates Deposition: The coordinates of the (+)-*cis-anti*-[BP]dA·dT 11-mer duplex have been deposited in the Protein Data Base, Brookhaven National Laboratory, Upton, New York, 11923, USA (acquisition number: 1axv), from whom copies can be obtained.

SUPPORTING INFORMATION AVAILABLE

Five tables are provided listing the complete exchangeable and nonexchangeable proton chemical shifts, goodness of fit data following distance-restrained DUPLEX refinement, comparison of experimental distance restraints with corresponding values in relaxation matrix refined structures, and pseudorotation and glycosidic torsion angles for the (+)-*cis-anti*-[BP]dA·dT 11-mer duplex. A figure showing the distance-restrained DUPLEX structures of the central segment of the (+)-*cis-anti*-[BP]dA·dT 11-mer duplex is also included.

REFERENCES

1. Harvey, R. G. (1991) *Polycyclic Aromatic Hydrocarbons: Chemistry and Carcinogenicity*, Cambridge University Press,
2. Grimmer, G. (1993) *Proc. 13th Internat. Symp. Polynuclear Aromatic Hydrocarbons*, (Garrigues, L., and Lamotte, M., Eds.), Gordon and Breach Science Publishers, Langhorne PA, pp 31−41.
3. Perrin, J. L., Poirot, N., Liska, P., Hanras, C., Theinpont, A., and Felix, G. (1993) *Proc. 13th Internat. Symp. Polynuclear Aromatic Hydrocarbons*, (Garrigues, P., and Lamotte, M., Eds.), Gordon and Breach Science Publishers, Langhorne, PA, pp 337−346.
4. Buening, M. K., Wislocki, P. G., Levin, W., Yagi, H., Thakker, D. R., Akagi, H., Koreeda, M., Jerina, D. M., and Conney, A. H. (1978) *Proc. Natl. Acad. Sci. U.S.A. 75*, 5358−5361.
5. Slaga, T. J., Bracken, W. J., Gleason, G., Levin, W., Yagi, H., Jerina, D. M., and Conney, A. H. (1979) *Cancer Res. 39*, 67−71.
6. Meehan, T., and Straub, K. (1979) *Nature 277*, 410−412.
7. Cheng, S. C., Hilton, B. D., Roman, J. M., and Dipple, A. (1989) *Chem. Res. Toxicol. 2*, 334−340.
8. Dipple, A., Pigott, M. A., Agarwal, S. K., Yagi, H., Sayer, J. M., and Jerina, D. M. (1989) *Nature 327*, 535−536.
9. Misra, B., Amin, S., and Hecht, S. S. (1992) *Chem. Res. Toxicol. 5*, 248−254.
10. Ralston, S. L., Seidel, A., Luch, A., Platt, K. I., and Baird, W. M. (1995) *Carcinogenesis 16*, 2899−2907.
11. Wood, A. W., Chang, R. L., Levin, W., Yagi, H., Thakker, D. R., Jerina, D. M., and Conney, A. H. (1977) *Biochem. Biophys. Res. Commun. 77*, 1389−1396.
12. Stevens, C. W., Bouck, N., Burgess, J. A., and Fahl, W. E. (1985) *Mutation Res. 152*, 5−14.
13. Brookes, P., and Osborne, M. R. (1982) *Carcinogenesis 3*, 1223−1226.
14. Rodriguez, H., and Loechler, E. L. (1993) *Biochemistry 32*, 1759−1769.
15. Wei, S. J. C., Chang, R. L., Wong, C. Q., Bhachech, N., Cui, X. X., Hennig, E., Yagi, H., Sayer, J. M., Jerina, D. M., Preston, B. D., and Conney, A. H. (1991) *Proc. Natl. Acad. Scis. USA. 88*, 11227−11230.
16. Wei, S. J. C., Chang, R. L., Bachech, N., Cui, X. X., Merkler, K. A., Wong, C. Q., Hennig, E., Yagi, H., Jerina, D. M., and Conney, A. H. (1993) *Cancer Res. 53*, 3294−3301.
17. Wei, S.-J. C., Chang, R. L., Hennig, E., Cui, X. X., Merkler, K. A., Wong, C.-Q., Yagi, H., and Conney, A. H. (1994) *Carcinogenesis 15*, 1729−1735.
18. Henning, E. E., Conney, A. H., and Wei, S.-J. (1995) *Cancer Res. 55*, 1550−1558.
19. Harris, C. C. (1991) *Cancer Res. (Suppl.) 51*, 5023s-5044s.
20. Vogelstein, B., and Kinzler, K. W. (1992) *Nature 355*, 209−210.
21. Zou, Y., Liu, T., Geacintov, N. E., and Van Houten, B. (1995) *Biochemistry 34*, 13582−13593.
22. Geacintov, N. E., Cosman, M., Hingerty, B. E., Amin, S., Broyde, S., and Patel, D. J. (1997) *Chem. Res. Toxicol. 10*, 111−146.
23. Cosman, M., Fiala, R., Hingerty, B., Laryea, A., Lee, H., Harvey, R. G., Amin, S., Geacintov, N. E., Broyde, S., and Patel, D. J. (1993) *Biochemistry 32*, 12488−12497.
24. Cosman, M., Laryea, A., Fiala, R., Hingerty, B. E., Amin, S., Geacintov, N. E., Broyde, S., and Patel, D. J. (1995) *Biochemistry 34*, 1295−1307.
25. Yeh, H. J. C., Sayer, J. M., Liu, X., Altieri, A. S., Byrd, R. A., Lakshman, M. K., Yagi, H., Schurter, E. J., Gorenstein, D. G., and Jerina, D. M. (1995) *Biochemistry 34*, 13570−13581.
26. Schwartz, J. L., Rice, J. S., Luxon, B. A., Sayer, J. M., Xie, G., Yeh, H. J. C., Liu, X., Jerina, D. M., and Gorenstein, D. G. (1997) *Biochemistry, 36*, 11069−11076.
27. Zegar, I. S., Kim, S. J., Johansen, T. N., Harris, C. M., Harris, T. M., and Stone, M. P. (1996) *Biochemistry 35*, 6212−6224.
28. Schurter, E. J., Yeh, H. J. C., Sayer, J. M., Lakshman, M. K., Yagi, H., Jerina, D. M., and Gorenstein, D. G. (1995) *Biochemistry 34*, 1364−1375.
29. Cosman, M., de los Santos, C., Fiala, R., Hingerty, B. E., Singh, S., Ibanez, V., Margulis, L. A., Live, D., Geacintov, N. E., Broyde, S., and Patel, D. J. (1992) *Proc. Natl. Acad. Sci. U.S.A. 89*, 1914−1918.
30. de los Santos, C., Cosman, M., Hingerty, B. E., Ibanez, V., Margulis, L. A., Geacintov, N. E., Broyde, S., and Patel, D. J. (1992) *Biochemistry 31*, 5245−5252.
31. Cosman, M., de los Santos, C., Fiala, R., Hingerty, B. E., Ibanez, V., Luna, E., Harvey, R. G., Geacintov, N. E., Broyde, S., and Patel, D. (1993) *Biochemistry 32*, 4145−4155.
32. Cosman, M., Hingerty, B. E., Luneva. N., Amin, S., Geacintov, N. E., Broyde, S., and Patel, D. J. (1996) *Biochemistry 35*, 9850−9863.
33. Marion, D., Ikura, M., Tschudin, R., and Bax, A. (1989) *J. Magn. Reson. 85*, 393−399.
34. Sklenar, V., Miyashiro, H., Zon, G., Miles, H. T., and Bax, A. (1986) *FEBS Lett. 208*, 94−98.
35. van de Ven, F. J., and Hilbers, C. W. (1988) *Eur. J. Biochem. 178*, 1−38.
36. Hingerty, B. E., Figueroa, S., Hayden, T., and Broyde, S. (1989) *Biopolymers 28*, 1195−1222.
37. Taylor, E. R., and Olson, W. K. (1983) *Biopolymers 22*, 2667−2702.
38. Brunger, A. T. (1992) *X-Plor: A System for X-ray Crystallography and NMR.* (New Haven and London: Yale University Press).
39. Patel, D. J., Shapiro, L., and Hare, D. (1987) *Annu. Rev. Biophys. Biophys. Chem. 16*, 423−454.
40. Arnott, S., Bond, P. J., Selsing, E., and Smith, P. J. (1976) *Nucleic Acids Res. 3*, 2459−2470.
41. Gorin, A. A., Zhurkin, V. B., and Olson, W. K. (1995) *J. Mol. Biol. 247*, 34−48.
42. Schurter, E. J., Sayer, J. M., Oh-hara, T., Yeh, H. C. J., Yagi, H., Luxon, B. A., Jerina, D. M., and Gorenstein, D. G. (1995) *Biochemistry 34*, 9009−9020.
43. Feng, B., Gorin, A., Kolbanovskiy, A., Hingerty, B. E., Geacintov, N. E., Broyde, S., and Patel, D. J. (1997) *Biochemistry 36*, 13780−13790.

Mao et al.

44. Hess, T. M., Gunz, D., Luneva, N., Geacintov, N. E., and Naegeli, H. (1997) *Mol. Cell. Biol. 17*, 7069−7076.
45. Chary, P., Latham, G. J., Robberson, D. L., Kim, S. J., Han, S., Harris, C. M., Harris, T. M., and Lloyd, R. S. (1995) *J. Biol. Chem. 270*, 4990−5000.
46. Chary, P., and Lloyd, R. S. (1995) *Nucleic Acids Res. 23*, 1398−1405.
47. Chary, P., and Lloyd, R. S. (1996). *Chem. Res. Toxicol. 9*, 409−417.
48. Christner, D. F., Lakshman, M. K., Sayer, J. M., Jerina, D. M., and Dipple, D. M. (1994) *Biochemistry 33*, 14297−14305.
49. Kraulis, P. J. (1991) *J. Appl. Crystallogr. 24*, 946−950.